DOI: 10.1111/cgf.13114

EUROGRAPHICS 2017 / L. Barthe and B. Benes
(Guest Editors)

Volume 36 (2017), Number 2

Flow-Induced Inertial Steady Vector Field Topology

Tobias Günther and Markus Gross

Computer Graphics Laboratory, ETH Zurich

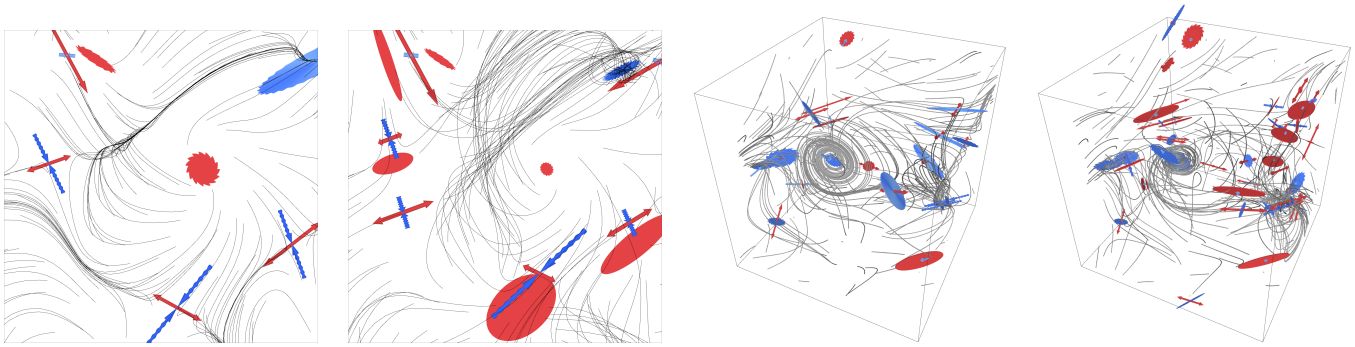

Model I: $d_p = 100\,\mu m$ **Model II**: $R = 1$, $St = 0.2$ **Model I**: $d_p = 100\,\mu m$ **Model II**: $R = 1$, $St = 0.2$

Figure 1: *Critical points in 2D and 3D flows for two different particle models. In contrast to massless flows, inertial particles might oscillate.*

Abstract

Traditionally, vector field visualization is concerned with 2D and 3D flows. Yet, many concepts can be extended to general dynamical systems, including the higher-dimensional problem of modeling the motion of finite-sized objects in fluids. In the steady case, the trajectories of these so-called inertial particles appear as tangent curves of a 4D or 6D vector field. These higher-dimensional flows are difficult to map to lower-dimensional spaces, which makes their visualization a challenging problem. We focus on vector field topology, which allows scientists to study asymptotic particle behavior. As recent work on the 2D case has shown, both extraction and classification of isolated critical points depend on the underlying particle model. In this paper, we aim for a model-independent classification technique, which we apply to two different particle models in not only 2D, but also 3D cases. We show that the classification can be done by performing an eigenanalysis of the spatial derivatives' velocity subspace of the higher-dimensional 4D or 6D flow. We construct glyphs that depict not only the types of critical points, but also encode the directional information given by the eigenvectors. We show that the eigenvalues and eigenvectors of the inertial phase space have sufficient symmetries and structure so that they can be depicted in 2D or 3D, instead of 4D or 6D.

Categories and Subject Descriptors (according to ACM CCS): I.3.3 [Computer Graphics]: Picture/Image Generation—Line and curve generation

1. Introduction

Flow visualization helps to gain insights into large and complex scientific vector field data. Typically, the analysis is limited to (un)steady 2D and 3D flows, which describe many natural physical phenomena such as the motion of gases or fluids. Many ideas and concepts can be extended to inertial systems, i.e., systems in which particles have a finite size and are subject to inertia. They are of great importance in a number of scientific disciplines, such as engineering (brown-out), biology (jellyfish feeding), meteorology (sediment transport), or physics (spacecraft navigation). These so-called inertial particles have not only a position, but also a velocity vector. The rate of how both variables change is described by a second-order ordinary differential equation, which can be interpreted as a higher-dimensional vector field, e.g., (un)steady flows in 4D or 6D. This means for instance, in every point of a 6D domain, there is a 6-dimensional vector. This forms a large amount of data, which introduces a number of challenges, both computationally and perceptually. Flow visualization has proven to be a good candidate for the visual analysis of such problems.

This paper deals with steady flow-induced inertial systems, i.e., settings in which finite-sized objects are carried by a steady underlying air or fluid flow. One way to approach this high-dimensional problem is to focus on topology, since it is a compact description of asymptotic behavior. Recently, Günther and Theisel [GT16a] have shown that the critical points (in dynamical systems these are also known as fixed points, stationary points or singularities) of a certain simple inertial system can be classified by the eigenvalues of the Jacobian of the underlying 2D air flow. Such a classification, however, depends on the underlying particle model and has to be revisited for every other equation of motion. In this paper, we extend their work in a number of aspects. Our contributions are the following:

- We regard the recent inertial flow visualization literature in terms of particle model dependence and discuss the generalization of inertial flow visualization concepts.
- We extract steady topology of flow-induced inertial systems not only for 2D but also for 3D underlying flows.
- We classify inertial critical points for two different particle models, and propose a model-independent method in which both appear as special cases.
- We utilize dynamical systems theory to identify *oscillation* around strongly attracting critical points.
- We derive simple closed-forms of the inertial eigenvectors and observe their properties and structure.
- We design a glyph that encodes directional information for the visualization of inertial critical points.

2. Related Work

In this section, we emphasize the role of vector field topology in traditional flow visualization. Afterward, we review recent work on inertial flows in terms of independence of the equation of motion.

2.1. Vector Field Topology

Topology is one of the most fundamental aspects of vector field analysis. In their seminal work, Helman and Hesselink [HH89, HH91] introduced topology to the visualization community, including the classification of first-order critical points, separatrices starting at saddles and attachment/detachment points at no-slip boundaries. Higher-order critical points [SKMR98], boundary switches [dLvL99], closed separatrices [WS01], saddle connectors [TWHS03] and boundary switch connectors [WTHS04a] extended the understanding of the topological skeleton. Vector field topology found numerous applications to smooth [WJE01], compress [LRR00, TRS03], model [The02, WTHS04b], or edit [CML*07] vector fields using Morse decomposition [CMLZ08]. For further reading, we refer to Weinkauf [Wei08] and the reports of Laramee et al. [LHZP07], Pobitzer et al. [PPF*11], Wang et al. [WWL16] and Heine et al. [HLH*16]. In this paper, we study the topology of inertial flows.

2.2. Inertial Particles in Visualization

Inertial particle motion is governed by an equation of motion, which can be described as a higher-dimensional vector field. In dynamical systems theory, the domain in which these vector fields are defined is called *phase space* and the trajectory of an inertial particle (i.e., the temporal evolution of the particle state) is simply a tangent curve in it. Inertial particles are important in many scientific areas, such as sand saltation modeling [SL99], soiling of cars [RSBE01], visual obscuration in helicopter landing maneuvers [SGL10, SBL11, KGRK14], formation of rain [Bor11], predator-prey movement in jellyfish feeding [PD09, SPH11] or spacecraft navigation [SBHH15]. Depending on the application, different assumptions are made. Thus, the higher-dimensional vector field that governs the particle motion is different for every equation of motion.

Tailored Analysis. On the one hand, restricting the view to a very particular particle model allows the user to study its unique properties, e.g., inertial vortex corelines [GT14]. Starting with simple models is also an essential step in the research process, where we later try to extend and generalize. An example is the extension of inertial critical point classification [GT16a] to other equations of motion, as done in this paper, or the extraction of so-called influence curves [GT16c] in more general inertial particle models [GT17]. Influence curves recover the origin of an inertial particle. This is useful, since traditional backward integration in flow-induced inertial systems is numerically very difficult [MBZ06, HS08].

Local Abstraction. On the other hand, we strive for general concepts to achieve broad applicability in not only flow-induced systems (particles carried with fluids), but also in gravitational systems (planetary systems). One approach is to introduce an abstract acceleration variable in the equation of motion [SJJ*17]. Depending on the application, acceleration could be calculated from an underlying fluid or from mass bodies (e.g., restricted three-body problem [SHT11], or general multi-body problems [SBHH15]). We follow a similar approach for the inherently local classification of inertial critical points. Instead of introducing an abstract variable in the higher-dimensional vector field, we introduce abstract variables in the Jacobian.

Integration-based Abstraction. Another approach is the definition of an abstract inertial flow map, which maps a seed location/velocity to the target location/velocity that is reached after integration for a certain duration. This approach was used for integration-based concepts, such as inertial integral curves [GKKT13], the determination of stable sets [GT16a], or derived quantities such as multiplicity maps [SJJ*17] or singular flow map gradients [GT16b]. Based on the flow map, finite-time Lyapunov exponents (FTLE) can be defined, which measure the spatial separation of nearby-released inertial particles [SH09, PD09]. Aside from spatial separation, also the separation in the full phase space [GPPMn15] or in its subspaces [SJJ*17] can be measured. Inertial backward FTLE was calculated by Sapsis et al. [SPH11], based on an ODE that captures the movement on attracting manifolds [HS08]. However, the movement of larger particles becomes instable in areas of high strain [SH08], driving them away from the manifold on which the ODE is valid. More recently, Günther and Theisel [GT17] applied influence curves to this problem, showing agreement with inertial particle attractors, which were previously compared with massless FTLE [SBR15]. Raben et al. [RRV14] computed FTLE for both tracer particles and inertial particles from experimental trajectories.

In some cases, the inertial flow map is required to have additional properties. For instance in [GT15], separation in parameter-dependent flow maps was studied, here, with respect to mass. The

integration-based influence curve extractor [GT16c] requires the flow map gradient to be invertible. This limitation was addressed by [GT16b], who, however, require a discretization of the flow map.

Visual Mappings. The reduction to lower-dimensional spaces was also of interest. Günther and Theisel [GT16a] used glyphs to encode stable sets for varying initial positions and velocities in underlying 2D flows. In [GT16c], they also used glyphs to depict the particle velocities that are observed at certain locations in the domain. Sagristà et al. [SJJ*17] overlaid quantities measured in the spatial subspace and the velocity subspace, and proposed to use stacked visualizations. In some cases, the extracted features turn out to be structures that can be searched in the domain of the underlying flow, such as vortex corelines [GT14] or critical points [GT16a].

3. Equations of Motion and Their Derivatives

In this section, we describe the two inertial particle models that will be used throughout this paper. Given is a steady n-D flow $\mathbf{u}(\mathbf{x})$ with $n \in \{2,3\}$ and its Jacobian matrix $\mathbf{J} = \nabla\mathbf{u}$.

Model I. Crowe et al. [CST98] modeled the motion of small spherical objects in fluids by the governing inertial particle model:

$$\tilde{\mathbf{u}}(\mathbf{x},\mathbf{v}) = \frac{\mathrm{d}}{\mathrm{d}\tau}\begin{pmatrix}\mathbf{x}\\ \mathbf{v}\end{pmatrix} = \begin{pmatrix}\mathbf{v}\\ \frac{\mathbf{u}(\mathbf{x})-\mathbf{v}}{r} + \mathbf{g}\end{pmatrix} \tag{1}$$

where r is the so-called *response time* (or *relaxation time*), which depends on particle diameter d_p, particle density ρ_p and the viscosity of the surrounding air μ:

$$r = \frac{d_p^2\,\rho_p}{18\,\mu} \tag{2}$$

This model was used for instance in [SGL10, PSGC11, KGRK14, CGP*10, BBC*11]. In this paper, we set as particle density ρ_p the density of dry sand, i.e., $\rho_p = 1600\,kg/m^3$. The diameter d_p was set between $30\,\mu m$ and $500\,\mu m$. The surrounding medium was assumed to be air, thus the viscosity was set to $\mu = 1.532 \times 10^{-5}\,kg/(m\cdot s)$.

The Jacobian of the inertial flow contains all first-order derivatives and is later used to characterize the types of critical points. For the particle model in Eq. (1) the Jacobian is [GT16a]:

$$\tilde{\mathbf{J}}(\mathbf{x},\mathbf{v}) = \begin{pmatrix}\mathbf{0} & \mathbf{I}\\ \frac{1}{r}\mathbf{J} & -\frac{1}{r}\mathbf{I}\end{pmatrix} \tag{3}$$

This model assumes that the particle density is much higher than the density of the surrounding air, e.g., as with sand particles in air.

Model II. A more general model that is also frequently used in the CFD literature [HS08, BTT02, BCPP00, VdMG06, SBR15] incorporates the density ratio of inertial particles and the surrounding medium, which removes one assumption from the previous model and thereby allows scientists to include buoyancy effects. The governing ODE is given for steady underlying flows by:

$$\tilde{\mathbf{u}}(\mathbf{x},\mathbf{v}) = \frac{\mathrm{d}}{\mathrm{d}\tau}\begin{pmatrix}\mathbf{x}\\ \mathbf{v}\end{pmatrix} = \begin{pmatrix}\mathbf{v}\\ \frac{R}{St}(\mathbf{u}(\mathbf{x})-\mathbf{v}) + \frac{3R}{2}\frac{D\mathbf{u}(\mathbf{x})}{D\tau} + (1-\frac{3R}{2})\mathbf{g}\end{pmatrix} \tag{4}$$

with $\frac{D\mathbf{u}(\mathbf{x})}{D\tau} = \nabla\mathbf{u}\cdot\mathbf{u} = \mathbf{J}\mathbf{u}$, St is the Stokes number ($St \to 0$ for massless particles), and ρ_f and ρ_p are the densities of the surrounding air and the inertial particles, respectively. Their density ratio R is:

$$R = \frac{2\rho_f}{\rho_f + 2\rho_p} \tag{5}$$

The equations (1) and (4) are fairly similar. Both include the term $(\mathbf{u}(\mathbf{x})-\mathbf{v})$, which lets inertial particles try to align their own velocity vector with the underlying flow. The scale factors r and R/St determine how quickly the inertial particles respond to changes in the underlying flow. While in Eq. (1) gravity was simply added, Eq. (4) performs a linear blend between flow acceleration and gravity, which is determined by the density ratio R. The Jacobian matrix of this inertial particle model has the form:

$$\tilde{\mathbf{J}}(\mathbf{x},\mathbf{v}) = \begin{pmatrix}\mathbf{0} & \mathbf{I}\\ \frac{R}{St}\mathbf{J} + \frac{3R}{2}\nabla(\mathbf{J}\mathbf{u}) & -\frac{R}{St}\mathbf{I}\end{pmatrix} \tag{6}$$

4. Inertial Steady Vector Field Topology

In the following sections, we discuss the location, classification and visualization of inertial critical points in 2D and 3D steady flows.

4.1. Location of Inertial Critical Points

In traditional vector field topology, critical points (also known as stagnation points or fixed points) are locations where any asymptotic particle motion stops, since there, the velocity is zero [HH89, HH91]. In inertial flows, critical points exist as well. Similar to the massless case, these are locations where the inertial flow is $\tilde{\mathbf{u}} = \mathbf{0}$. Applied to the two inertial particle models, the following conditions arise:

Model I, cf. Eq. (1): $\mathbf{u} + r\mathbf{g} = \mathbf{0}$
Model II, cf. Eq. (4): $\frac{R}{St}\mathbf{u} + \frac{3R}{2}\mathbf{J}\mathbf{u} + (1-\frac{3R}{2})\mathbf{g} = \mathbf{0}$

Both conditions can be evaluated in n-D. The first condition was reported in [GT16a] and is implemented by adding $r\mathbf{g}$ to the underlying flow $\mathbf{u}$ prior to a search for critical points. The second condition additionally involves the computation of the Jacobian, but is likewise implemented as search for critical points in an n-D flow.

As with massless flows, inertial critical points are classified by an eigenanalysis of the Jacobian matrix $\tilde{\mathbf{J}}$, in this case a $2n \times 2n$ matrix. If an eigenvalue is positive, particles are repelled in the direction of the corresponding eigenvector; if it is negative, particles are attracted. It turns out that the $2n$ eigenvalues can be calculated analytically from the n eigenvalues of a certain $n \times n$ matrix. This not only eases the computation of the eigenvalues, it further allows us to make observations about their symmetry and signs. For the eigenvalues of the inertial Jacobian in Eq. (3), this was done by [GT16a].

In this paper, we generalize the eigenanalysis of the inertial Jacobian to the more general equation of motion in Eq. (4). Instead of rederiving from scratch, we propose a general scheme, in which both previously discussed particle models appear as special cases.

4.2. Classification of Inertial Critical Points

We have seen in the previous section that the inertial flows (1) and (4), and their Jacobians (3) and (6) have a similar form. In the following, we will name the response coefficient κ (note that $\kappa > 0$)

and introduce a matrix $\mathbf{K}$ in the spatial gradient of the velocity subspace. The inertial Jacobians can then both be described as:

$$\tilde{\mathbf{J}}(\mathbf{x},\mathbf{v}) = \begin{pmatrix} \mathbf{0} & \mathbf{I} \\ \frac{1}{\kappa}\mathbf{K} & -\frac{1}{\kappa}\mathbf{I} \end{pmatrix} \tag{7}$$

by setting

Eq. (3): $\kappa = r$ $\quad \mathbf{K} = \mathbf{J}$

Eq. (6): $\kappa = St/R$ $\quad \mathbf{K} = \mathbf{J} + \frac{3St}{2}\nabla(\mathbf{Ju})$

Further, let e_i be the n eigenvalues and $\mathbf{c}_i$ be the corresponding n eigenvectors of matrix $\mathbf{K}$, with $i \in \{1,\dots,n\}$. Note that in model I in Eq. (3), these are the eigenvalues and eigenvectors of Jacobian $\mathbf{J}$ of the underlying air flow $\mathbf{u}$. Günther and Theisel [GT16a] used this relation to relate critical points of the underlying massless flow to their inertial counterparts. In more complicated particle models, the classification cannot be done by only considering the eigenvalues of $\mathbf{J}$ in the underlying air flow.

For each eigenvalue e_i of the matrix $\mathbf{K}$, there are two eigenvalues $f_{i,1}$ and $f_{i,2}$ in the inertial Jacobian (7):

$$f_{i,1} = \frac{-1-\sqrt{1+4\kappa e_i}}{2\kappa}, \quad f_{i,2} = \frac{-1+\sqrt{1+4\kappa e_i}}{2\kappa} \tag{8}$$

This was shown by [GT16a] in 2D for model I. As outlined in the appendix, Eq. (8) holds generally, including the 3D case, and when applied to the respective matrix $\mathbf{K}$, even for more general models.

Necessary Attraction. Günther and Theisel [GT16a] concluded that one eigenvalue of each pair has a negative sign, since their mean is a negative real-valued number:

$$(f_{i,1} + f_{i,2})/2 = -1/(2\kappa) \tag{9}$$

Thus, one eigenvalue of each pair must be smaller than the mean, having a negative real part, w.l.o.g., let this be $f_{i,1}$:

$$Re(f_{i,1}) \leq -1/(2\kappa) < 0 \tag{10}$$

Due to the guaranteed presence of negative real parts, there is always an attracting part in the inertial flow and traditional sources (all eigenvalues are positive) no longer exist. From Eq. (8), we conclude that this property holds similarly in 3D and in the inertial flow in Eq. (4). Further, we can see that each eigenvalue pair is located diametrically opposite around this mean. Along with the property that complex eigenvalues appear in pairs of complex conjugates, this creates symmetry in the complex plane. See Fig. 2 for an illustration.

Sign of Second Eigenvalue. According to Eq. (10), the eigenvalue $f_{i,1}$ is always negative. To classify the inertial critical point, we have to determine when $f_{i,2}$ becomes negative. According to [GT16a] this depends on the eigenvalue e_i of the underlying flow:

$$Re(e_i) < -\kappa\, Im(e_i)^2 \tag{11}$$

Thus, when the underlying flow is attracting and when the rotation (imaginary part) is too strong, then inertial particles are repelled away from the critical point, since $f_{i,2}$ is positive. This is intuitive, since in this case inertia has a stronger impact on the particle trajectory than the weak attraction. An example is shown later in Fig. 9.

Complex Eigenvalues. In traditional massless flows, complex eigenvalues of the Jacobian indicate swirling motion. In inertial systems, there is not only swirling motion, but also *oscillation*.

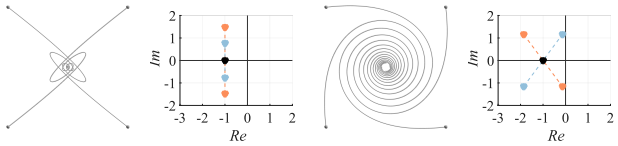

Figure 2: *Oscillation (left) and swirling motion (right). In both cases, eigenvalues $f_{1,1}, f_{1,2}$ (●), and $f_{2,1}, f_{2,2}$ (●) of the inertial Jacobian are complex, and are located diametrically opposite around the real-valued constant center $-1/(2\kappa)$ (●), here shown for $\kappa = 0.5$. In contrast to [GT16a], we distinguish these cases.*

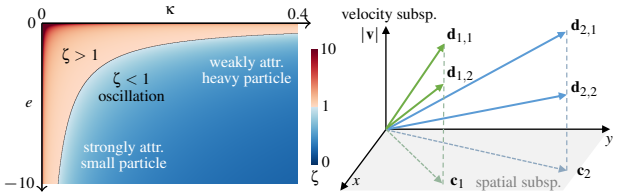

(a) *Damping ratio ζ, Eq. (12)* **(b)** *Projection of eigenvectors $\mathbf{d}_{i,j}$*

Figure 3: *Plot of damping ratio ζ, and projection of $2n$ inertial eigenvectors $\mathbf{d}_{i,1}$ and $\mathbf{d}_{i,2}$ into spatial subspace gives n vectors $\mathbf{c}_i$.*

Generally, the so-called *damping ratio* ζ characterizes, whether a dynamical system oscillates [AH12]. In our case (see appendix):

$$\zeta = \frac{1}{2\kappa\sqrt{-\frac{e}{\kappa}}} \tag{12}$$

Damping ratio ζ depends on the response coefficient κ (particle size) and the attracting eigenvalue $e < 0$. The classification is as follows:

- $\zeta > 1$: **Overdamped**. This is a movement toward the critical point without oscillation. Overshooting can occur, but the eigenvalues $f_{i,1}$ and $f_{i,2}$ are real-valued.
- $\zeta < 1$: **Underdamped**. Trajectories are oscillating around the critical point, but decay toward it for $\zeta \neq 0$. Eigenvalues $f_{i,1}$ and $f_{i,2}$ are complex.
- $\zeta = 1$: **Critically damped**. Threshold between the previous cases. This is typically the fastest way to reach the critical point.

Günther and Theisel [GT16a] found that the eigenvalues $f_{i,1}$ and $f_{i,2}$ of the inertial Jacobian are complex if

$$Re(e_i) < -1/(4\kappa) \tag{13}$$

This is obtained for $Im(e_i) = 0$, when inserting (12) into $\zeta < 1$. Thus, the condition in Eq. (13) distinguishes for underlying non-swirling flows, whether inertial particles are oscillating. Fig. 3a visualizes the damping ratio ζ and shows that oscillation occurs for weakly-attracted heavy particles and strongly-attracted small particles.

Properties of Eigenvectors. All relevant properties that are required to classify inertial critical points can be deduced from the eigenvalues of $\mathbf{K}$. But it still leaves us wondering, how do six eigenvectors span the 6D phase space?

The eigenvectors of the inertial flow can be calculated from the eigenvectors $\mathbf{c}_i$ of matrix $\mathbf{K}$ in the following way (see appendix):

$$\tilde{\mathbf{d}}_{i,1} = \begin{pmatrix} \mathbf{c}_i \\ f_{i,1}\,\mathbf{c}_i \end{pmatrix}, \quad \tilde{\mathbf{d}}_{i,2} = \begin{pmatrix} \mathbf{c}_i \\ f_{i,2}\,\mathbf{c}_i \end{pmatrix} \tag{14}$$

This means, for each eigenvector $\mathbf{c}_i$, there are two eigenvectors $\tilde{\mathbf{d}}_{i,1}$

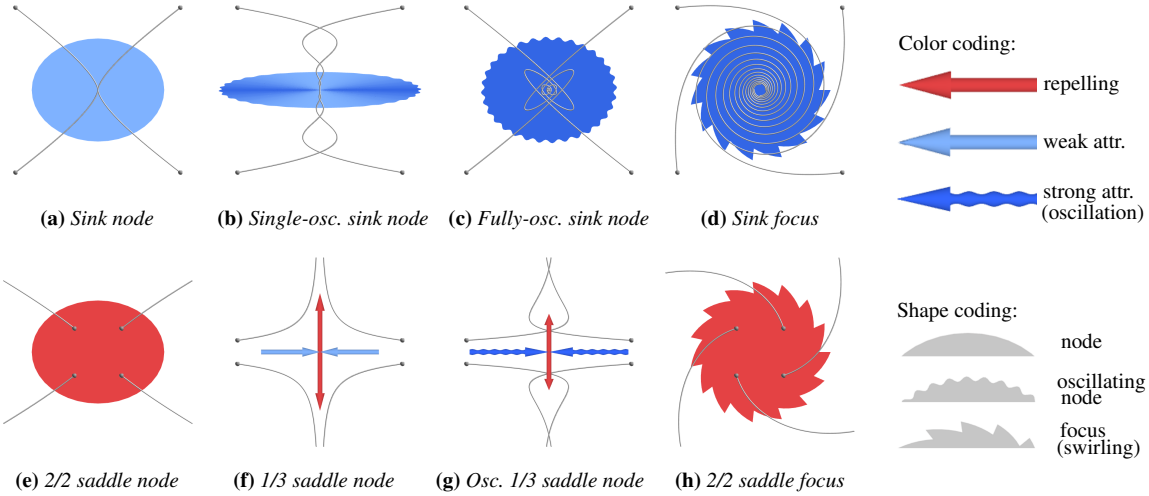

(a) *Sink node* **(b)** *Single-osc. sink node* **(c)** *Fully-osc. sink node* **(d)** *Sink focus*

(e) *2/2 saddle node* **(f)** *1/3 saddle node* **(g)** *Osc. 1/3 saddle node* **(h)** *2/2 saddle focus*

Figure 4: *Overview of all 8 types of inertial 2D critical points. Inertial streamlines (gray) were released from rest with* $\mathbf{v}_0 = \mathbf{0}$.

and $\tilde{\mathbf{d}}_{i,2}$ in the inertial flow. In Eq. (14), we see that the spatial subspace of each pair of eigenvectors is exactly the eigenvector $\mathbf{c}_i$ of matrix $\mathbf{K}$. Thus, if we project all $2n$ inertial eigenvectors into the spatial subspace, we do not end up with $2n$ vectors, but only n, since each vector occurred twice, see Fig. 3b. Further, the velocity subspace only contains scaled versions of the underlying eigenvectors $\mathbf{c}_i$. Thus, all directional information can be shown by n vectors. This insight leads us to the design of a glyph, described in Section 4.3.

Difference between Oscillation and Swirling. Günther and Theisel [GT16a] distinguished inertial critical points only by the number of complex eigenvalues in the inertial flow. While oscillation and swirling are both rotations in the inertial phase space, inertial particles behave differently in the spatial subspace for $Im(e_i) = 0$ (weak attraction vs. oscillation) and $Im(e_i) \neq 0$ (swirling motion) when Eq. (13) holds. Thus, it matters whether the eigenvalues e_i of the underlying flow are complex. This can be seen in the way how the swirling plane (i.e., the plane in which the rotation occurs) is spanned in the inertial phase space. Swirling planes are generally spanned by eigenvectors that correspond to complex conjugate eigenvalues. Let z^* be the complex conjugate of z.

- In the case $Im(e_i) = 0$ with Eq. (13), the eigenvalues computed from e_i are complex conjugates: $f_{i,1} = f_{i,2}^*$. This means, the swirling motion occurs in the plane that is spanned by the eigenvectors corresponding to $f_{i,1}$ and $f_{i,2}$, which were computed from *one* eigenvalue e_i. Looking at Eq. (14), we see that for both the spatial subspace of the eigenvector is $\mathbf{c}_i$, which does not span a plane but only a line. This is an *oscillation*.
- For the case $Im(e_i) \neq 0$, let e_k be the complex conjugate of e_i, i.e., $e_i = e_k^*$. Then, $f_{i,1} = f_{k,1}^*$ and $f_{i,2} = f_{k,2}^*$ form the complex conjugate pairs. In this case, the spatial subspace of two swirling planes is spanned by eigenvectors $\mathbf{c}_i$ and $\mathbf{c}_k$ that were computed from *two* different eigenvalues e_i and e_k. This is a *swirling motion*.

Fig. 2 illustrates inertial particle trajectories for both cases. Case $Im(e_i) = 0$ exhibits an oscillation, whereas $Im(e_i) \neq 0$ clearly has swirling characteristics. In contrast to [GT16a], we distinguish between these cases in our classification and visualization.

4.3. Visualization of Inertial Critical Points

Glyphs are a common tool to encode multi-dimensional data in space [BKC*13]. Seltzer and Kindlmann [SK16] and Gerrits et al. [GRT17] recently proposed glyphs for general asymmetric second-order tensors in 2D and 3D. They formulated lists of desirable properties that a glyph should fulfill (invariance under isometric domain transformations and scaling, direct encoding of real eigenvalues and eigenvectors, uniqueness and continuity). Gerrits et al. [GRT17] emphasized that certain properties might be less important in the application at hand. In terms of critical points, for instance, we are interested in topologically different behavior. Therefore, we would like the transition between topologically different behaviors (non-swirling vs. swirling, weak attraction vs. oscillation) to be visible, i.e., discontinuous. We use the glyphs of Theisel et al. [TWHS03] as a basis, see Weinkauf [Wei08] for applications of them. We refer to Borgo et al. [BKC*13] for further design criteria.

Color Coding. Similar to previous critical point glyphs [TWHS03], we use color to encode the attracting/repelling behavior. For a given particle model in an underlying n-D flow, we calculate for each inertial critical point the velocity subspace matrix $\mathbf{K}$ according to Eq. (7), which has n eigenvalues. By inserting them into Eq. (8), we compute the $2n$ eigenvalues $f_{i,1}, f_{i,2}$ with $i \in \{1, ..., n\}$ of the inertial flow. From Eq. (10) we know that half the eigenvalues are definitely negative, w.l.o.g. let this be $f_{i,1}$. Thus, in order to determine the attracting/repelling behavior of the inertial critical point, we only have to observe the remaining n eigenvalues $f_{i,2}$ and thus, we color-code only them. By inspecting e_i using Eq. (11), we can distinguish between attracting and repelling behavior. In addition, using Eq. (13) we determine that strongly attracting nodes exhibit oscillation. Thus, for nodes, we further distinguish between weak and strong attraction, see Table 1 for the classification and Fig. 4 for examples. Swirling motion and oscillation are encoded by the same color, since both have in common that eigenvalues of the inertial system are complex. Thus, for (●) we have $Im(f_{i,1}) = Im(f_{i,2}) = 0$ and in case of (●) we have $Im(f_{i,1}) \neq 0, Im(f_{i,2}) \neq 0$.

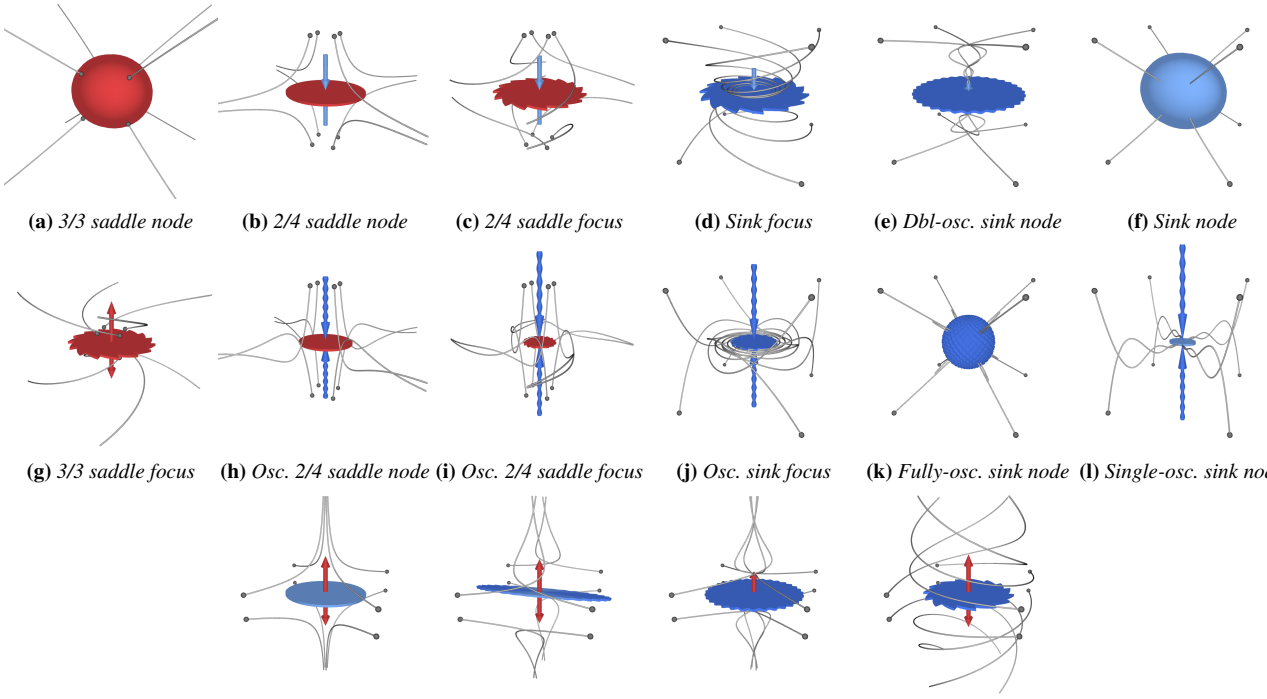

(a) *3/3 saddle node* **(b)** *2/4 saddle node* **(c)** *2/4 saddle focus* **(d)** *Sink focus* **(e)** *Dbl-osc. sink node* **(f)** *Sink node*

(g) *3/3 saddle focus* **(h)** *Osc. 2/4 saddle node* **(i)** *Osc. 2/4 saddle focus* **(j)** *Osc. sink focus* **(k)** *Fully-osc. sink node* **(l)** *Single-osc. sink node*

(m) *1/5 saddle node* **(n)** *Single-osc. 1/5 saddle node* **(o)** *Dbl-osc. 1/5 saddle node* **(p)** *1/5 saddle focus*

Figure 5: *Overview of all 16 types of inertial 3D critical points. Inertial streamlines (gray) were released from rest with* $\mathbf{v}_0 = \mathbf{0}$.

● **Repelling:**	$Re(e_i) \geq -\kappa\, Im(e_i)^2$
● **Weak attraction:**	$Im(e_i) = 0 \;\wedge\; -\frac{1}{4\kappa} < Re(e_i) < 0$
● **Strong attraction:**	$Im(e_i) = 0 \;\wedge\; Re(e_i) \leq -\frac{1}{4\kappa}$ $Im(e_i) \neq 0 \;\wedge\; Re(e_i) < -\kappa\, Im(e_i)^2$

Table 1: *Color coding*

Shape Coding. Similar to [TWHS03], we use shape to distinguish between nodes (non-swirling) and foci (swirling motion), see Fig. 4. Thereby, arrows depict a single eigenvector $\mathbf{c}_i$, whereas the discs are spanned by two eigenvectors. For (fully-oscillating) sink nodes and 3/3 saddle nodes, we use an ellipsoid, which is oriented according to the three eigenvectors. Nodes have a smooth boundary, whereas foci have a zig-zag boundary. In addition to this, we introduce a new shape type that encodes oscillation, i.e., a sine-shaped boundary, which is applied to spheres, disks and arrows alike. The classification is done as follows:

Node:	$Im(e_i) = 0 \;\wedge\; Re(e_i) > -\frac{1}{4\kappa}$
Oscillation:	$Im(e_i) = 0 \;\wedge\; Re(e_i) \leq -\frac{1}{4\kappa}$
Focus:	$Im(e_i) \neq 0$

Table 2: *Shape coding*

Glyphs in 2D and 3D. A complete overview of all 8 glyph types in underlying 2D flows is given in Fig. 4. Fig. 5 illustrates the 16 different kinds of inertial critical points in underlying 3D flows. We extended the naming conventions of [GT16a] to incorporate oscillation, but otherwise followed their example. A 1/5 saddle for instance, has one positive and five negative eigenvalues, whereas a 2/4 saddle has two positives and four negatives. In all images, we released inertial streamlines with $\mathbf{v}_0 = \mathbf{0}$ at the gray spheres to show the flow behavior in the vicinity of inertial critical points. Aside from swirling motion, oscillation is apparent as well. We introduce the notion of single-oscillating, double-oscillating and fully-oscillating sink nodes, which declares the number of underlying eigenvalues that cause oscillation. In case of single-oscillating sink nodes for instance, Fig. 4b, we linearly blend the shape and color between weak and strong attraction. The plane of the discs is chosen according to the corresponding eigenvectors of the pair of complex conjugate eigenvalues e_i (swirling) or is spanned by the eigenvectors that have eigenvalues e_i with the same sign (saddles).

Regarding the aforementioned list of desirable glyph properties, our glyphs are not unique, since swirling strength (rotation) is not encoded. Gerrits et al. [GRT17] encode this via color, which would be possible with our glyphs as well. Since we want to investigate the interpretation of different types of complex eigenvalues, we chose to use color to distinguish between weak attraction and strong attraction (in addition to representing oscillation with different shape).

5. Results

In the following, we extract and visualize inertial critical points in a number of 2D and 3D vector fields. While the experiments in magnetic fields are rather synthetic, they showcase our method in flows that are more complicated than the frequently-used analytic

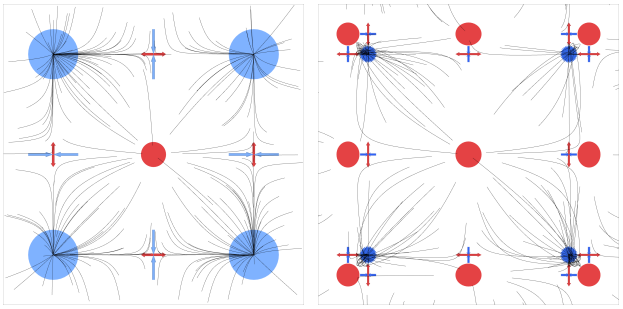

Model I: $d_p = 100\,\mu m$ **Model II**: $R = 0.2$, $St = 0.2$

Figure 6: *Different particle models applied to the* NINECP *flow. Model II contains more critical points and exhibits oscillation.*

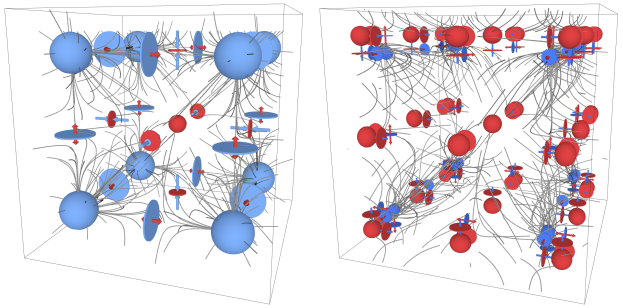

Model I: $d_p = 100\,\mu m$ **Model II**: $R = 0.2$, $St = 0.2$

Figure 7: *Over-damped (left) and under-damped (right) inertial trajectories in the* TWENTYSEVENCP *flow, shown for both models.*

ones. We also conduct experiments in fluid flows, which allow us to infer insights, e.g., on particle trapping by vortices. We refer to the accompanying video for animations of varying model parameters.

Random. Fig. 1 shows random underlying 2D and 3D flows, in which we released inertial particles using both models. The 2D case shows oscillating streamlines. While model I captures the motion of aerosol particles, model II is also able to trace bubbles ($R > 2/3$).

NineCP. A more structured test case contains nine critical points that are laid out on a regular grid [GT16a]. The underlying flow is:

$$\mathbf{u}(x,y) = \begin{pmatrix} x(1-x)(1+x) \\ y(1-y)(1+y) \end{pmatrix} \tag{15}$$

In Fig. 6, inertial streamlines visualize the asymptotic motion toward the inertial critical points. When the impact of the acceleration term in Eq. (4) is large, model II may contain additional critical points. In this experiment, all attracting behavior is under-damped for aerosol particles ($R < 2/3$), which causes oscillation.

TwentySevenCP. A direct 3D extension of the previous case is:

$$\mathbf{u}(x,y,z) = \begin{pmatrix} x(1-x)(1+x) \\ y(1-y)(1+y) \\ z(1-z)(1+z) \end{pmatrix} \tag{16}$$

Fig. 7 shows streamlines in this completely swirling-free test case. For the given particles in model II, all attracting components have complex eigenvalues in the inertial Jacobian, indicating oscillation.

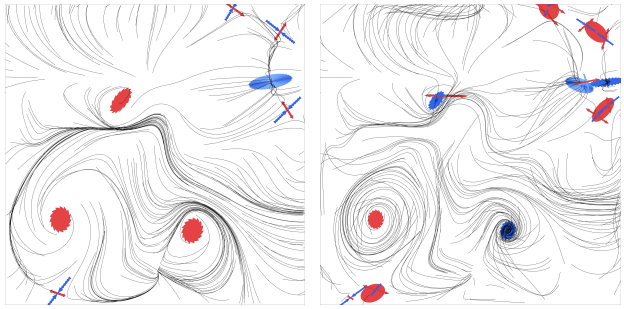

Model I: $d_p = 250\,\mu m$ **Model II**: $R = 0.8$, $St = 0.5$

Figure 8: *Aerosol particles (left) and bubbles (right) in the* BORROMEAN. *Note the oscillation at the top-right corner of model I.*

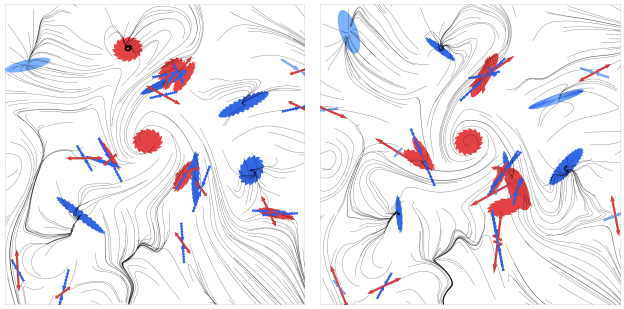

Model I: $d_p = 160\,\mu m$ **Model II**: $R = 2/3$, $St = 1$

Figure 9: *Impact of gravity in* TREFOIL *flow. Particles are pulled down (model I) or are unaffected by it (neutrally-buoyant, model II). Further note the closed orbit forming around the top-most 2/2 saddle in model I. Here, the underlying flow contains a sink, but the rotational strength forces inertial particles to spin away.*

Borromean. We observed inertial motion in a magnetic field, in which field lines are interlocked in the shape of Borromean rings that decay over time [CB11]. Fig. 8 shows a slice of one time step that was used in [GT16a]. Our glyphs represent the strongly attracting line in the top-right corner in model I well. The image of model II shows the slightly more turbulent motion of bubbles ($R > 2/3$).

Trefoil. The trefoil is another magnetic field from [CB11] that was used in [GT16a], and Fig. 9 depicts a 2D slice of it. In this experiment, we added a synthetic gravity of $\mathbf{g} = (0,-2)^T$ that pulls the particles down in model I. As a reference, model II uses neutrally-buoyant particles ($R = 2/3$), on which gravity has no impact. This

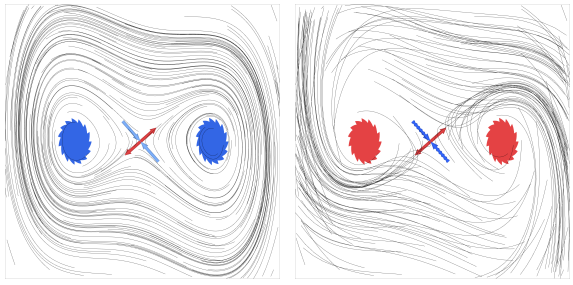

Model I: $d_p = 160\,\mu m$ **Model I**: $d_p = 400\,\mu m$

Figure 10: *Larger particles have more inertia and are repelled away from attracting foci of the underlying* DUFFING *flow.*

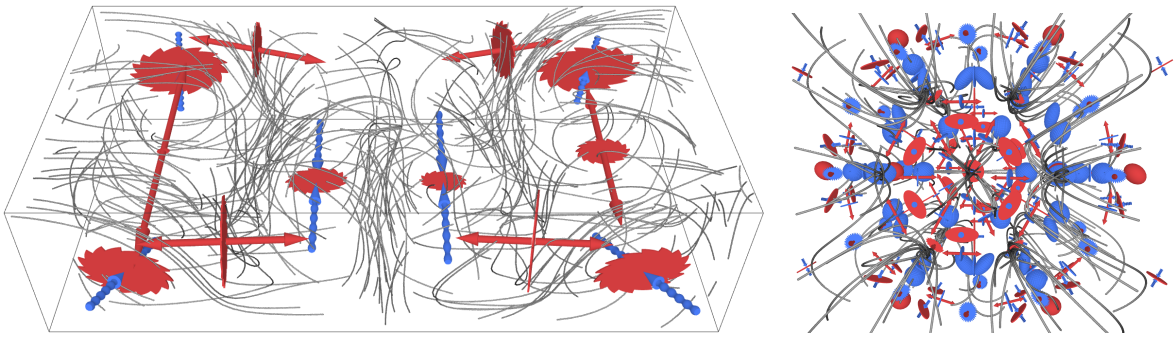

Model I: $d_p = 300\,\mu m$ **Model II**: $R = 0.04, St = 0.2$

Figure 11: *Heavy aerosol particles in the* BENARD *flow (left) cluster between the vortices, since inertia drives them away from the vortex cores. In the* BENZENE *field (right) trajectories oscillate around the fully-oscillating sinks. Note that there is no swirling motion.*

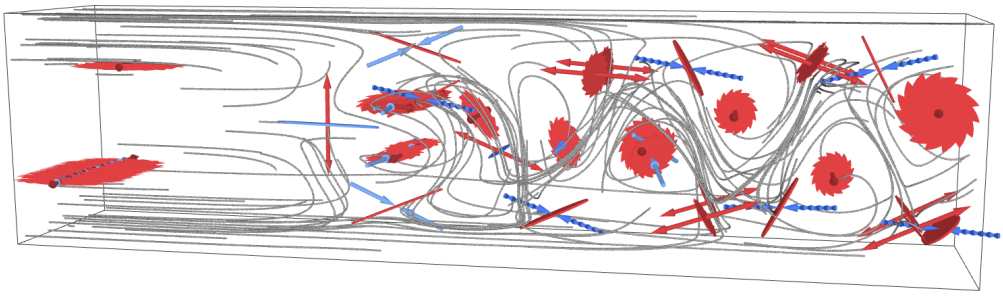

Model I: $d_p = 500\,\mu m$

Figure 12: *In the* SQUARE CYLINDER *flow, heavy inertial particles are not trapped by the vortices of the von-Kármán vortex street.*

aside, note the top-most 2/2 saddle in model I. The trajectories are moving toward it. In fact, the underlying flow contains a sink. But, its rotational strength causes inertial particles to drift away from the critical point, leading them onto a closed orbit that surrounds it.

Duffing. The forced-damped Duffing oscillator in Fig. 10 gives another example of inertial particles being repelled away from underlying attracting foci due to rotational strength. Here, the impact of particle size is illustrated. Larger particles have more inertia, which is also why the critical point in the middle becomes oscillating. The underlying vector field originates from a dynamical system, which was studied in [HS11] and appeared in [GT15, GT16a].

Bénard. Another 3D example is given in the Rayleigh-Bénard convection, simulated with NaSt3DGP, shown in Fig. 11 (left). The inertial particles are so large that every rotating motion in this flow causes them to be repelled outward. As a consequence, trajectories tend to cluster in the void spaces between the critical points. Density can be measured by preferential particle concentration [GT17].

Benzene. The underlying normalized potential field of a benzene molecule [ZSH96] contains a large number of critical points. In Fig. 11 (right), we scaled the domain significantly up to create a synthetic test case, in which we extracted inertial critical points for aerosol particles. The trajectories exhibit strong oscillation, which is especially apparent at the oscillating 2/4 saddle node at the center and the fully-oscillating sink nodes surrounding it.

Square Cylinder. The square cylinder flow was simulated by Camarri et al. [CSBI05] and contains a vortex street in the wake of an obstacle. The resampled version of the flow was provided by Tino Weinkauf, and is shown in Fig. 12. Similar to the Bénard flow, no critical point can trap inertial particles, since they are too heavy and inertia repels them away. Instead, the inertial particles cluster in the void spaces between the vortices of the vortex street.

Impact of Initial Velocity. It is important to note that the glyphs show the *asymptotic* particle behavior. Depending on the initial velocity, particles might overshoot critical points or perform detours before aligning with the underlying flow. An example is shown in Fig. 13, where particles are released with different initial velocities near an attracting node (neither oscillation nor swirling). Over time the impact of initial velocity vanishes and the attraction prevails.

Performance and Robustness. Since the search for inertial critical points can be reduced to an n-D problem, the extraction performance is similar to the traditional massless case. With model I, critical point extraction and classification took for 2D data sets $< 2\,ms$ and for 3D flows $50 - 500\,ms$ with an Intel i7-6700HQ CPU. The only exception was the BENZENE field with $1.2\,sec$. The extraction in

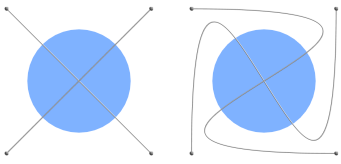

Figure 13: *Inertial particles are released in the same flow from the same position, but with different initial velocity.*

model II was generally slower, since here additionally the gradient of the acceleration $\nabla(\mathbf{Ju})$ is calculated, see Eq. (7). (In analytic flows $1.3\times$ slower, in real-world flows $3-5\times$ slower.) The gradient of the acceleration requires second-order derivatives of the vector field. In numerical real-world data, their extraction can be sensitive to noise, which is an inherent limitation of particle models that require higher-order derivatives. The effect can be seen in the video.

6. Conclusions

In this paper, we extracted, classified and visualized critical points of inertial particles in steady 2D and 3D underlying flows. We identified eight different types of critical points in 2D and sixteen critical points in 3D underlying flows. In particular, we extended the work of Günther and Theisel [GT16a] to 3D, generalized it to another particle model, identified oscillation and included directional information by the eigenvectors of the inertial system. The classification of inertial critical points usually depends on the particle model. By studying the Jacobians of two flow-induced inertial models, we derived a common Jacobian template, in which both appear as special cases. For generalization, we devised a classification method that is applicable to any particle model that fits the template. This is also our limitation. So far, even simple gravitational models, such as the circular restricted three-body problem do not fit the template. In the future, we would like to extend our method to gravitational systems.

Acknowledgements: We wish to thank Holger Theisel for the insightful discussions on theory and glyph design.

Appendix

In the following, we briefly sketch the derivations of eigenvalues, damping and eigenvectors of the inertial Jacobian, Eq. (8).

Eigenvalues of Inertial Jacobian. Inertial motion can be described as second-order ODE of the form:

$$m\frac{\mathrm{d}^2\mathbf{x}}{\mathrm{d}t^2}+b\frac{\mathrm{d}\mathbf{x}}{\mathrm{d}t}-k\mathbf{x}=\mathbf{f}(t) \tag{17}$$

In Eqs. (1) and (4) the particle motion was equivalently formulated as two coupled first-order ODEs. The stability (attracting/repelling behavior) of such a system is studied by its homogeneous part, i.e., without external forces $\mathbf{f}(t)$ such as gravity $\mathbf{g}$. For our model in Eq. (7), we have $k=-\mathbf{K}/\kappa$. We separately study the behavior in the direction of the eigenvectors, thus we consider $\mathbf{x}$ to be an eigenvector of $\mathbf{K}$, and get $\mathbf{Kx}=e\mathbf{x}$. The coefficients then become:

$$m=1 \quad b=\frac{1}{\kappa} \quad k=-\frac{e}{\kappa} \tag{18}$$

The corresponding characteristic equation is [AH12]:

$$m\,f^2+b\,f-k=0 \tag{19}$$

For (18), its roots are precisely the eigenvalues in (8). Thus it turns out that Eq. (8) holds for every eigenvalue of $\mathbf{K}$, including the 3D case.

Damping Ratio. For a dynamical system of the form (17), the damping ratio has a closed-form expression [AH12]. For (18) it is:

$$\zeta=\frac{\text{actual damping}}{\text{critical damping}}=\frac{b}{2\sqrt{km}}=\frac{\frac{1}{\kappa}}{2\sqrt{-\frac{e}{\kappa}}}=\frac{1}{2\kappa\sqrt{-\frac{e}{\kappa}}} \tag{20}$$

Eigenvectors of Inertial Jacobian. Let e and $\mathbf{c}$ be an eigenvalue and eigenvector of matrix $\mathbf{K}$, respectively, i.e., $\mathbf{Kc}=e\mathbf{c}$. Further, let f and $\tilde{\mathbf{d}}$ be eigenvalue and eigenvector of matrix $\tilde{\mathbf{J}}$. Next, we show that eigenvector $\tilde{\mathbf{d}}$ is (14):

$$\tilde{\mathbf{d}}=\begin{pmatrix}\mathbf{c}\\ f\,\mathbf{c}\end{pmatrix} \tag{21}$$

by showing that $\tilde{\mathbf{J}}\tilde{\mathbf{d}}=f\tilde{\mathbf{d}}$, using $\mathbf{Kc}=e\mathbf{c}$ and Eq. (8):

$$\tilde{\mathbf{J}}\tilde{\mathbf{d}}=\begin{pmatrix}\mathbf{c}\,f\\ \frac{\mathbf{Kc}}{\kappa}-\frac{\mathbf{c}\,f}{\kappa}\end{pmatrix}=\begin{pmatrix}\mathbf{c}\,f\\ \frac{\mathbf{c}(e-f)}{\kappa}\end{pmatrix}=\begin{pmatrix}\mathbf{c}\,f\\ \mathbf{c}\,f^2\end{pmatrix}=f\tilde{\mathbf{d}} \tag{22}$$

References

[AH12] ALCIATORE D. G., HISTAND M. B.: *Introduction to Mechatronics and Measurement Systems*, 4 ed. McGraw Hill, 2012. 4, 9

[BBC*11] BEC J., BIFERALE L., CENCINI M., LANOTTE A. S., TOSCHI F.: Spatial and velocity statistics of inertial particles in turbulent flows. *Journal of Physics: Conference Series 333*, 1 (2011), 012003. 3

[BCPP00] BABIANO A., CARTWRIGHT J. H. E., PIRO O., PROVENZALE A.: Dynamics of a small neutrally buoyant sphere in a fluid and targeting in Hamiltonian systems. *Phys. Rev. Lett. 84* (Jun 2000), 5764–5767. 3

[BKC*13] BORGO R., KEHRER J., CHUNG D. H. S., MAGUIRE E., LARAMEE R. S., HAUSER H., WARD M., CHEN M.: Glyph-based visualization: Foundations, design guidelines, techniques and applications. In *Eurographics State of the Art Reports (STARs)* (2013), pp. 39–63. 5

[Bor11] BORDÁS R.: *Optical measurements in disperse two-phase flows: Application to rain formation in cumulus clouds*. PhD thesis, University of Magdeburg, 2011. 2

[BTT02] BENCZIK I. J., TOROCZKAI Z., TÉL T.: Selective sensitivity of open chaotic flows on inertial tracer advection: Catching particles with a stick. *Phys. Rev. Lett. 89* (Sep 2002), 164501. 3

[CB11] CANDELARESI S., BRANDENBURG A.: Decay of helical and nonhelical magnetic knots. *Phys. Rev. E 84* (2011), 016406. 7

[CGP*10] CASCIOLA C. M., GUALTIERI P., PICANO F., SARDINA G., TROIANI G.: Dynamics of inertial particles in free jets. *Physica Scripta 2010*, T142 (2010), 014001. 3

[CML*07] CHEN G., MISCHAIKOW K., LARAMEE R. S., PILARCZYK P., ZHANG E.: Vector field editing and periodic orbit extraction using morse decomposition. *IEEE Transactions on Visualization and Computer Graphics 13*, 4 (2007), 769–785. 2

[CMLZ08] CHEN G., MISCHAIKOW K., LARAMEE R. S., ZHANG E.: Efficient morse decompositions of vector fields. *IEEE Transactions on Visualization and Computer Graphics 14*, 4 (July 2008), 848–862. 2

[CSBI05] CAMARRI S., SALVETTI M.-V., BUFFONI M., IOLLO A.: Simulation of the three-dimensional flow around a square cylinder between parallel walls at moderate Reynolds numbers. In *XVII Congresso di Meccanica Teorica ed Applicata* (2005). 8

[CST98] CROWE C., SOMMERFIELD M., TSUJI Y.: *Multiphase Flows with Droplets and Particles*. CRC Press, 1998. 3

[dLvL99] DE LEEUW W., VAN LIERE R.: Collapsing flow topology using area metrics. In *Proc. Visualization* (1999), pp. 349–354. 2

[GKKT13] GÜNTHER T., KUHN A., KUTZ B., THEISEL H.: Mass-dependent integral curves in unsteady vector fields. *Computer Graphics Forum (Proc. EuroVis) 32*, 3 (2013), 211–220. 2

[GPPMn15] GARABOA-PAZ D., PÉREZ-MUÑUZURI V.: A method to calculate finite-time Lyapunov exponents for inertial particles in incompressible flows. *Nonlin. Proc. in Geophys. 22*, 5 (2015), 571–577. 2

[GRT17] GERRITS T., RÖSSL C., THEISEL H.: Glyphs for general second-order 2D and 3D tensors. *IEEE Trans. Visualization and Computer Graphics (Proc. IEEE SciVis 2016) 23*, 1 (2017), to appear. 5, 6

[GT14] GÜNTHER T., THEISEL H.: Vortex cores of inertial particles. *IEEE Transactions on Visualization and Computer Graphics (Proc. IEEE Scientific Visualization) 20*, 12 (2014), 2535–2544. 2, 3

[GT15] GÜNTHER T., THEISEL H.: Finite-time mass separation for comparative visualizations of inertial particles. *Computer Graphics Forum (Proc. EuroVis) 34*, 3 (2015), 471–480. 2, 8

[GT16a] GÜNTHER T., THEISEL H.: Inertial steady 2D vector field topology. *Computer Graphics Forum (Proc. Eurographics) 35*, 2 (2016), 455–466. 2, 3, 4, 5, 6, 7, 8, 9

[GT16b] GÜNTHER T., THEISEL H.: Singularities of the inertial flow map gradient. *Proc. Vision, Modeling, and Visualization (VMV)* (2016), 69–76. 2, 3

[GT16c] GÜNTHER T., THEISEL H.: Source inversion by forward integration in inertial flows. *Computer Graphics Forum (Proc. EuroVis) 35*, 3 (2016), 371–380. 2, 3

[GT17] GÜNTHER T., THEISEL H.: Backward finite-time Lyapunov exponents in inertial flows. *IEEE Trans. on Visualization and Computer Graphics (Proc. IEEE SciVis 2016) 23*, 1 (2017), to appear. 2, 8

[HH89] HELMAN J. L., HESSELINK L.: Representation and display of vector field topology in fluid flow data sets. *Computer 22*, 8 (1989), 27–36. 2, 3

[HH91] HELMAN J. L., HESSELINK L.: Visualizing vector field topology in fluid flows. *IEEE Comp. Graph. & Applications 11* (1991), 36–46. 2, 3

[HLH*16] HEINE C., LEITTE H., HLAWITSCHKA M., IURICICH F., DE FLORIANI L., SCHEUERMANN G., HAGEN H., GARTH C.: A survey of topology-based methods in visualization. *Computer Graphics Forum (Proc. EuroVis - STAR) 35*, 3 (2016), 643–667. 2

[HS08] HALLER G., SAPSIS T.: Where do inertial particles go in fluid flows? *Physica D: Nonlinear Phenomena 237* (May 2008), 573–583. 2, 3

[HS11] HALLER G., SAPSIS T.: Lagrangian coherent structures and the smallest finite-time Lyapunov exponent. *Chaos 21*, 2 (2011), 023115. 8

[KGRK14] KUTZ B. M., GÜNTHER T., RUMPF A., KUHN A.: Numerical examination of a model rotor in brownout conditions. In *Proceedings of the American Helicopter Society* (2014), no. AHS2014-000343. 2, 3

[LHZP07] LARAMEE R., HAUSER H., ZHAO L., POST F.: Topology-based flow visualization, the state of the art. In *Topology-based Methods in Visualization*, Hauser H., Hagen H., Theisel H., (Eds.), Mathematics and Visualization. Springer Berlin Heidelberg, 2007, pp. 1–19. 2

[LRR00] LODHA S., RENTERIA J., ROSKIN K.: Topology preserving compression of 2D vector fields. In *Proc. IEEE Visualization* (2000), pp. 343–350. 2

[MBZ06] MOGRABI E., BAR-ZIV E.: On the asymptotic solution of the Maxey-Riley equation. *Physics of Fluids 18*, 5 (2006). 2

[PD09] PENG J., DABIRI J. O.: Transport of inertial particles by Lagrangian coherent structures: Application to predator–prey interaction in jellyfish feeding. *Journal of Fluid Mechanics 623* (3 2009), 75–84. 2

[PPF*11] POBITZER A., PEIKERT R., FUCHS R., SCHINDLER B., KUHN A., THEISEL H., MATKOVIC K., HAUSER H.: The state of the art in topology-based visualization of unsteady flow. *Computer Graphics Forum 30*, 6 (2011), 1789–1811. 2

[PSGC11] PICANO F., SARDINA G., GUALTIERI P., CASCIOLA C.: DNS of a free turbulent jet laden with small inertial particles. In *Direct and Large-Eddy Simulation VIII*, vol. 15 of *ERCOFTAC Series*. Springer Netherlands, 2011, pp. 189–194. 3

[RRV14] RABEN S. G., ROSS S. D., VLACHOS P. P.: Experimental determination of three-dimensional finite-time Lyapunov exponents in multi-component flows. *Experiments in Fluids 55*, 10 (2014), 1–6. 2

[RSBE01] ROETTGER S., SCHULZ M., BARTELHEIMER W., ERTL T.: Automotive soiling simulation based on massive particle tracing. In *Data Visualization 2001*, Eurographics. Springer Vienna, 2001, pp. 309–317. 2

[SBHH15] SHORT C. R., BLAZEVSKI D., HOWELL K. C., HALLER G.: Stretching in phase space and applications in general nonautonomous multi-body problems. *Celestial Mechanics and Dynamical Astronomy 122* (2015), 213–238. 2

[SBL11] SYDNEY A., BAHARANI A., LEISHMAN J. G.: Understanding brownout using near-wall dual-phase flow measurements. In *Proc. American Helicopter Society, 67th Annual Forum* (May 2011). 2

[SBR15] SUDHARSAN M., BRUNTON S. L., RILEY J. J.: Lagrangian coherent structures and inertial particle dynamics. *ArXiv e-prints* (2015). 1512.05733. 2, 3

[SGL10] SYAL M., GOVINDARAJAN B., LEISHMAN J. G.: Mesoscale sediment tracking methodology to analyze brownout cloud developments. In *Proc. American Helicopter Society, 66th Annual Forum* (2010). 2, 3

[SH08] SAPSIS T., HALLER G.: Instabilities in the dynamics of neutrally buoyant particles. *Phys. Fluids 20* (2008), 017102. 2

[SH09] SAPSIS T. P., HALLER G.: Inertial particle dynamics in a hurricane. *Journal of the Atmospheric Sciences* (2009). 2

[SHT11] SHORT C., HOWELL K., TRICOCHE X.: Lagrangian coherent structures in the restricted three-body problem. In *Proc. AAS/AIAA Space Flight Mechanics Meeting* (2011), pp. 11–250. 2

[SJJ*17] SAGRISTÀ A., JORDAN S., JUST A., DIAS F., NONATO L. G., SADLO F.: Topological analysis of inertial dynamics. *IEEE Trans. on Vis. and Comp. Graph. (Proc. IEEE SciVis 2016) 23*, 1 (2017), to appear. 2, 3

[SK16] SELTZER N., KINDLMANN G.: Glyphs for asymmetric second-order 2D tensors. *Computer Graphics Forum (Proc. EuroVis) 35*, 3 (2016), 141–150. 5

[SKMR98] SCHEUERMANN G., KRUGER H., MENZEL M., ROCKWOOD A.: Visualizing nonlinear vector field topology. *IEEE Transactions on Visualization and Computer Graphics 4*, 2 (1998), 109–116. 2

[SL99] SHAO Y., LI A.: Numerical modelling of saltation in the atmospheric surface layer. *Boundary-Layer Meteor. 91* (1999), 199–225. 2

[SPH11] SAPSIS T., PENG J., HALLER G.: Instabilities on prey dynamics in jellyfish feeding. *Bull Math Biol. 73*, 8 (2011), 1841–1856. 2

[The02] THEISEL H.: Designing 2D vector fields of arbitrary topology. *Comp. Graphics Forum (Proc. Eurographics) 21*, 3 (2002), 595–604. 2

[TRS03] THEISEL H., RÖSSL C., SEIDEL H.-P.: Compression of 2D vector fields under guaranteed topology preservation. *Computer Graphics Forum (Proc. Eurographics) 22*, 3 (2003), 333–342. 2

[TWHS03] THEISEL H., WEINKAUF T., HEGE H.-C., SEIDEL H.-P.: Saddle connectors - an approach to visualizing the topological skeleton of complex 3D vector fields. In *Proc. IEEE Visualization* (2003), pp. 225–232. 2, 5, 6

[VdMG06] VILELA R. D., DE MOURA A. P. S., GREBOGI C.: Finite-size effects on open chaotic advection. *Phys. Rev. E 73* (2006), 026302. 3

[Wei08] WEINKAUF T.: *Extraction of Topological Structures in 2D and 3D Vector Fields*. PhD thesis, University Magdeburg, 2008. 2, 5

[WJE01] WESTERMANN R., JOHNSON C., ERTL T.: Topology-preserving smoothing of vector fields. *IEEE Transactions on Visualization and Computer Graphics 7*, 3 (2001), 222–229. 2

[WS01] WISCHGOLL T., SCHEUERMANN G.: Detection and visualization of closed streamlines in planar flows. *IEEE Transactions on Visualization and Computer Graphics 7*, 2 (2001), 165–172. 2

[WTHS04a] WEINKAUF T., THEISEL H., HEGE H.-C., SEIDEL H.-P.: Boundary switch connectors for topological visualization of complex 3D vector fields. In *VisSym* (2004), pp. 183–192. 2

[WTHS04b] WEINKAUF T., THEISEL H., HEGE H.-C., SEIDEL H.-P.: Topological construction and visualization of higher order 3D vector fields. *Computer Graphics Forum (Proc. EG) 23*, 3 (2004), 469–478. 2

[WWL16] WANG W., WANG W., LI S.: From numerics to combinatorics: a survey of topological methods for vector field visualization. *Journal of Visualization* (2016), 1–26. 2

[ZSH96] ZÖCKLER M., STALLING D., HEGE H.-C.: Interactive visualization of 3D vector fields using illuminated stream lines. In *IEEE Visualization* (1996), pp. 107–113. 8